DOI: 10.14529/jsfi250106

Modelling and Supercomputer Simulation of Hinged Rotor

Ilya V. Abalakin[1], *Vladimir G. Bobkov*[1], *Tatiana K. Kozubskaya*[1], *Aleksey V. Lipatov*[2]

The paper presents a computational technology of numerical simulation of turbulent flow over a hinged rotor on high-performance heterogeneous computer systems. A key part of the technology is the developed mathematical model describing the complex motions of triple-hinged rigid blades of a helicopter under the action of external and aerodynamic forces and its implementation using an original unstructured mesh-deformation algorithm. The mesh-deformation method exploits an auxiliary web-structured mesh with its elastic compression-expansion controlled by low-cost quasi-one-dimensional strand-based algorithms. The mechanics model is verified by solving the pendulum problems. To demonstrate the correctness of the developed techniques, the problems on taper stabilization and blade motion under cyclic control for model helicopter rotors are considered. All the presented computations are carried out using the code NOISEtte for solving aerodynamics and aeroacoustics problem. The code implements higher-accuracy methods of computational fluid dynamics on unstructured mixed-element meshes and operates with a high efficiency on modern supercomputers with arbitrary architectures including CPU cores and GPU accelerators.

Keywords: helicopter, rotor kinematics, cyclic control, flapping motion, taper stabilization, computational fluid dynamics, turbulent flows, unstructured mesh, mesh deformation, higher-accuracy method, CPU+GPU.

Introduction

Numerical simulations of turbulent flows generated by real helicopter rotors are the problems that require large computing resources and therefore modern high-performance supercomputers to solve them. The complexity of simulating non-stationary turbulent flows in such problems is aggravated by the need to correctly take into account the non-trivial mechanics of the hinged rotor blades. Nowadays efficient implementation of high-fidelity computational fluid dynamics for hinged rotors combined with proper blade mechanics presents a challenge to the global community involved in numerical simulation of helicopter problems. That is why among a huge number of publications devoted to numerical investigation of helicopter rotors and estimation of their aerodynamic and acoustic properties (see, for instance, [4, 17, 23–25]) only a few of them consider real hinged rotors in coupling with blade mechanics.

In most of papers on hinged rotors, the authors use the computational techniques offered by commercial CFD codes or even combinations of them. Thus, the CFD codes are often combined with MBDyn [1] and CAMRAD [16] packages, to provide the blade mechanics. The paper [14] studies the hinged rotor problem with the help of FINFLO solver for rotary wing applications.

The team of Prof. George Barakos from University of Glasgow U.K., one of the strongest university teams involved in helicopter research in Europe, develops their own software. Let us highlight the work [20] where they consider both blade cyclic control and flapping motions prescribed by the given laws. To achieve the target thrust coefficient, the special trimming method is used.

Another important phenomenon of hinged rotor is aeroelasticity of helicopter blades. Among the publications considering this feature there are, for instance, the papers [6] and [21]. However it appears difficult to combine it with well-developed CFD and blade mechanics.

[1]Keldysh Institute of Applied Mathematics, RAS, Moscow, Russian Federation
[2]Bauman Moscow State Technical University, Moscow, Russian Federation

In general, it can be said that to date no commonly accepted CFD platform has been developed for the numerical solution of the hinged rotor problem. In this situation, new efficient methods adapted to the rapidly growing performance of modern supercomputers are still in great demand.

A goal of this paper is to present a computational technology to simulate turbulent flows generated by helicopter rotors with three-hinged rigid blades in different flight modes. The developed methods are implemented within the code NOISEtte [5] for solving aerodynamics and aeroacoustics problems on unstructured mixed-element meshes. The proposed technology combines a turbulent flow model (among those from RANS to scale-resolving hybrid RANS-LES methods implemented in NOISEtte) with a novel mathematical description of blade mechanics and original numerical techniques to maintain the blade motions on a moving unstructured mesh.

The paper is organized as follows. Section 1 describes a coupled simulation of turbulent airflow and articulated blade dynamics in helicopter rotors, solved with mesh deformation across multiple reference frames. Section 2 presents mathematical models and numerical methods involved in the framework of turbulent flow simulation. Section 3 describes the models governing the blade mechanics and the corresponding numerical methods. Section 4 is devoted to the mesh deformation technique. Section 5 contains the numerical results. The Conclusion summarizes the results of the work.

1. General Scheme of Numerical Simulation of Hinged Rotor Problems

Numerical simulation of a helicopter rotor with articulated blades involves modeling the motion of each blade as its key component. The spatial position of the blade depends on the acting inertial forces caused by its rotation and externally given cyclic control, gravity and aerodynamic forces arising from the motion (i.e., rotation and forward motion) of it in the air. Accounting for aerodynamic forces requires the simulation of the flow near the helicopter rotor, and the aerodynamic forces themselves depend on the position of the blade.

Thus, the computation of the flow near a helicopter rotor and the motion of each rotor blade must be carried out jointly at a discrete time step within the selected model for describing the fluid and the model for the blade motion.

In helicopter applications, a liquid medium near rotors is viscous compressible turbulent flow of air. As a model for describing it, the Reynolds-averaged Navier–Stokes system of equations (RANS) closed by different turbulence models is widely used. It should be noted that, depending of the problem, the Euler or Navier–Stokes equations can be also applicable. The best description of turbulent flow is currently provided by scale-resolving hybrid RANS-LES (Large Eddy Simulation) models, however the implementation of these models requires high computational costs.

The mathematical model that determines the movement of the articulated blades of a helicopter rotor presents a system of nonlinear ordinary differential equations written in the form of the law of conservation of angular momentum.

The general algorithm for the joint solution of the gasdynamics equations and the equations of rotor blade motion at each discrete time step can be written as the following stages:

1. Determination of the pressure field from the simulation of flow over the helicopter rotor.

2. Calculation of the aerodynamic forces acting on the blade, basing on the pressure distribution on its surface.
3. Calculation of the blade displacement and determination of its new spatial position at a new time step.
4. Deformation of the computational mesh for making it consistent to the new blade position and preparation of initial information needed for computations at the next time step.
5. Returning to point 1.

The above algorithm involves three main processes: simulation of turbulent flow around the helicopter rotor, modeling of blade movements, and deformation of the computational mesh.

To simulate the turbulent flow around hinged rotor, to model the motion of its blades and to implement the corresponding mesh movement, it is convenient to consider the following different frames of reference (FR):

– *Helicopter frame of reference (HFR).* The origin of the FR coincides with the center of the rotor hub. The Oz axis is co-directed with the axis of rotation of the rotor shaft, the Ox axis is co-directed with the line of the zero-azimuth position of the blade downstream, the Oy axis complements the FR to the right-hand system. This FR can be also considered as absolute.
– *Rotating, non-inertial, frame of reference (RFR).* The origin of the FR coincides with the center of the rotor hub. The Oz axis is co-directed with the axis of rotation of the rotor shaft, the Ox axis is directed parallel to the longitudinal axis of the blade at zero angles of flapping and lagging, the Oy axis complements the FR to the right-hand system.
– *Blade, non-inertial, frame of reference (BFR).* Its description is given in detail in the section devoted to modeling the blade motion.

2. Mathematical Models and Numerical Methods for Turbulent Flow Simulation

2.1. Governing Equations

Let us model the viscous compressible gas flow by the RANS system of equations with Spalart–Allmaras (SA) turbulence model in the form of the conservation laws of mass, momentum and total energy. Consider these equations in an integral form suitable for implementing an arbitrary Lagrangian-Eulerian approach (ALE) for constructing numerical finite-volume schemes on moving meshes and/or in a non-inertial RFR. It is important to note here that in all the FR under consideration we use the flow velocity components determined in the absolute HFR. Below we designate the velocity in the HFR as “absolute velocity”.

When considering the RANS system in the RFR, the rotation of the axes of this FR occurs around the rotor shaft axis with a time-independent angular velocity vector $\boldsymbol{\omega}$ with magnitude equal to the rotation speed of the helicopter rotor. In contrast to the HFR case, the absolute velocity in the RFR is projected to the rotating axes which results in the appearance of an additional term responsible for the velocity turn in the governing gasdynamic equations. With this description, the streamlined rotor remains motionless, and the direction of the upstream flow changes dependently to the azimuthal angle $\psi = |\boldsymbol{\omega}|t$. Note that at the discretized level the linear tangential velocity $\boldsymbol{V}_\omega = \boldsymbol{\omega} \times \boldsymbol{r}$ of the blade rotation, where $\boldsymbol{r}$ is the radius-vector, can be interpreted as a stationary velocity of mesh movement in the HFR.

To write the system of Navier–Stokes equations in the form of conservation laws, we introduce the vector of conservative variables

$$\boldsymbol{Q} = (\rho,\ \rho\boldsymbol{u},\ E,\ \rho\tilde{\nu})^{\mathsf{T}}\,,$$

where $\boldsymbol{u} = (u_1, u_2, u_3)$ is the velocity vector in HFR, ρ is the density, $E = \rho\boldsymbol{u}^2/2 + \rho\varepsilon$ is the total energy, ε is the specific internal energy, $p = \rho\varepsilon\,(\gamma - 1)$ is the pressure defined by the ideal perfect gas state of equation, the constant γ is the specific ratio, $\tilde{\nu}$ is turbulent eddy viscosity.

Let $C(t)$ be the computational cell on a given mesh with volume $|C(t)|$ and $\overline{\boldsymbol{Q}}$ be the integral average of $\overline{\boldsymbol{Q}}(t)$ over this cell. Then

$$\frac{d}{dt}\int\limits_{C_i(t)} \boldsymbol{Q} dV = \frac{d\overline{\boldsymbol{Q}}_i\,|C_i(t)|}{dt}, \qquad |C_i(t)| = \int\limits_{C_i(t)} dV, \qquad \overline{\boldsymbol{Q}}_i = \frac{1}{|C_i(t)|}\int\limits_{C_i(t)} \boldsymbol{Q} dV$$

and the RANS system implementing ALE approach can be written as shown in [10] as

$$\begin{aligned}\frac{d\overline{\boldsymbol{Q}}_i\,|C_i(t)|}{dt} &+ \int\limits_{\partial C_i(t)} \mathcal{F}^C(\boldsymbol{Q})\cdot\boldsymbol{n}dS - \int\limits_{\partial C_i(t)} \boldsymbol{Q}\,(\boldsymbol{V}_c\cdot\boldsymbol{n})\,dS \\ &= \int\limits_{C_i(t)} \mathcal{F}^D(\boldsymbol{Q},\nabla\boldsymbol{Q})\,dV + \int\limits_{C_i(t)} \boldsymbol{S}(\boldsymbol{Q},\nabla\boldsymbol{Q})\,dV.\end{aligned} \tag{1}$$

Here $\partial C_i(t)$ is the boundary of cell, $\boldsymbol{n}$ is the unit external normal to the boundary $\partial C_i(t)$, $\boldsymbol{V}_c$ is the velocity of the moving-cell boundary. In general, when using the RFR, the boundary-cell velocity is the vector sum of the mesh deformation rate $\boldsymbol{V}_d$ and the linear tangential rotation velocity $\boldsymbol{V}_\omega$.

System (1) includes composite vectors $\mathcal{F}^C$ and $\mathcal{F}^D$, each component of which F_i^C and F_i^D in coordinate direction x_i $(i = 1, 2, 3)$ represents the convective transport and diffusion flux vectors, respectively.

The components of convective transport flux vector are given as functions of the physical variables ρ, $\boldsymbol{u}$, p:

$$F_i^C(\boldsymbol{Q}) = (\rho u_i, \rho\boldsymbol{u}u_i + p\boldsymbol{e}_i, (E+p)u_i, \rho\tilde{\nu}u_i)^{\mathsf{T}}\,,$$

where $\boldsymbol{e}_i = (\delta_{i1}, \delta_{i2}, \delta_{i3})^{\mathsf{T}}$ is the row-vector of the identity matrix and δ_{ij} is the Kronecker symbol. The diffusion flux vector is defined as a vector-function of physical variables and their gradients as

$$F_i^D(\boldsymbol{Q},\nabla\boldsymbol{Q}) = (0, \tau_{i1}, \tau_{i2}, \tau_{i3}, \tau_{ij}u_j + q_i, k_d(\nabla\rho\tilde{\nu})_i)^{\mathsf{T}}\,,$$

where the components of the viscous stress tensor τ_{ij}, the heat flux vector q_i, and the diffusion coefficient k_d are defined according to the RANS system with the closing SA model (see, for example, [3]).

Vector $S(\boldsymbol{Q},\nabla\boldsymbol{Q})$ is the source term describing the influence of the external forces that are not related to the transport of conservative variables $\boldsymbol{Q}$

$$\boldsymbol{S}(\boldsymbol{Q},\nabla\boldsymbol{Q}) = (0, -\rho(\boldsymbol{\omega}\times\boldsymbol{u}), 0, S_{SA})^{\mathsf{T}}\,,$$

where S_{SA} is the source term in the SA equation describing turbulence generation and turbulence destruction (a complete description can be found, for example, in [3]), the term $-\rho(\boldsymbol{\omega} \times \boldsymbol{u})$ in the momentum equation determines the velocity vector turn to the angle equal to $-|\boldsymbol{\omega}|t$ when using the RFR.

Note that when using a movable (deformable) computational mesh with the mesh velocity depending on time and spatial coordinates, it is necessary to recompute the new positions of all the nodes and rebuild the final (control) volumes at each time step. When using the RFR the mesh velocity does not depend on time so the geometry of the mesh elements does not change, and the mesh is transported as a rigid body together with the rotor.

2.2. Higher-Accuracy Quasi-One-Dimensional Reconstruction-Based Methods

To solve system (1) we use the CFD/CAA NOISEtte code [5] which exploits vertex-centered algorithms on unstructured mixed-element meshes. According to the NOISEtte framework for the discretization of the convective terms, the family of EBR (Edge-Based Reconstruction) finite-volume schemes is used [2, 7, 8]. A higher accuracy of EBR schemes is achieved thanks to the edge-based quasi-one-dimensional reconstruction of variables involved in the flux calculation according to one or another Riemann solver. For the problems considered in the paper, as a Riemann solver, we use the Roe method. For the discretization of the diffusion terms, the standard P1-Galerkin method and the method of averaged element splittings (AES) are used [9]. The time integration is implemented using the backward time differentiation formulas of the first and second orders. To solve the nonlinear algebraic systems, the Newton method is used. The corresponding linear systems are solved using the biconjugate gradient stabilized method.

2.3. Parallel Implementation

All the above mentioned models, methods and algorithms have effective and robust parallel implementation within the CFD/CAA NOISEtte code (see [5, 12]). The NOISEtte code is written in C++ using MPI, OpenMP and OpenCL frameworks for parallel implementation. It consists of a core computational library and connectable functional modules that are linked to console applications for preprocessing, running simulations, and postprocessing results. The code is designed to provide the maximum portability and can be used on Windows and Linux, on a wide range of computing systems from workstations to hybrid supercomputers. It has been tested on various computing architectures, including multicore CPUs (Intel, AMD, IBM, ARM, Elbrus), multi-core accelerators (Intel Xeon Phi KNC, KNL), GPUs (Intel, AMD, NVIDIA), systems on a chip combining central and graphics processors.

A parallel implementation of the computational algorithm is based on hierarchical multilevel model (see [12, 13]). At the top level, the MPI standard is used to couple multiple nodes of a cluster system. Then, the second-level mesh partitioning is used to further distribute the workload among computing devices of hybrid cluster nodes, such as CPUs and GPUs. MPI parallelization uses asynchronous, non-blocking exchanges and allows communications to be hidden behind computations to improve parallel efficiency, which is especially important for GPU computing. To reduce the data transfer overhead, multi-threaded message processing is used as well.

3. Mathematical Models and Numerical Methods for Rotor Mechanics

3.1. Description of Three-Hinged Blade and Its Kinematics

The hinged attachment of the blade implies the attachment of it to the hub by means of the following three hinges: 1) a flap hinge (FH) allowing the blade to move in the vertical plane (flapping motion); 2) a lag hinge (LH) allowing the blade to move in the horizontal plane (lagger motion); 3) and an pitch hinge (PH) allowing the blade to rotate around its longitudinal axis (pitching motion).

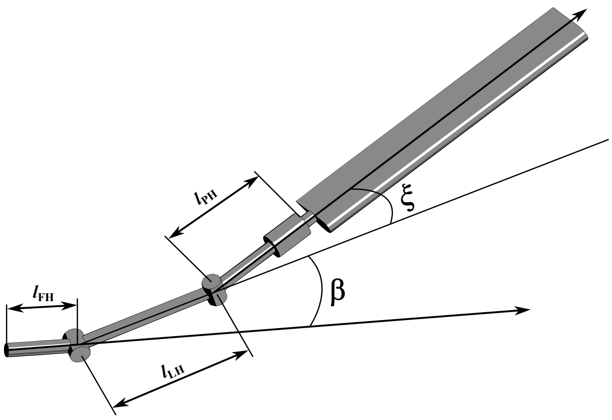

Figure 1. Schematic representation of an articulated blade

The sequence of hinges is specified as FH→LH→PH, with the distances between them defined as: l_{RH} is the distance from the hub center to the LH, l_{LH} is the distance from the FH to the LH and l_{PH} is the distance from the LH to the PH (see Fig. 1).

The modeling of the articulated blade motion is carried out under the following assumptions:

- The blade is considered an absolutely rigid body, meaning it does not deform under load.
- The mass of the blade is concentrated along its longitudinal axis to simplify the analysis of its motion.
- The moments created by the control system lever relative to the FH and LH are assumed to be zero, i.e., no external torques are applied at these hinges.
- The dimensions of the hinges are small compared to the blade which allows them to be treated as point connections.
- Only the blade has mass, the hinges and hub are considered massless.

The kinematics of the blade is determined by the following angular values:

- Flapping angle β is the angle between the plane of rotation of the rotor and the longitudinal axis of the blade.
- Lagging angle ξ is the angle between the plane passing through the azimuthal position of the blade (i.e., the plane perpendicular to the rotor's plane of rotation at a specific azimuth) and the longitudinal axis of the blade.
- Pitching angle φ is the angle between the chord of the blade section at $0.7R$ (where R is the radius of the rotor) and the plane of rotation of the rotor.

3.2. Blade Dynamics

The problem of determining the spatial position of the blade depending on the aerodynamic and inertial forces acting on it includes solving the equations for finding the angles β, ξ, φ under the following assumptions:

- The helicopter moves in forward flight mode, that is, in a straight line and at a constant velocity (a particular case is the hover mode).
- The blade control, or the change in its pitch angle φ, is determined by an externally specified control law

$$\varphi(\psi) = \varphi_0 + \varphi_1 \cos(\psi) + \varphi_2 \sin(\psi) + k_\beta \beta + k_\xi \xi, \tag{2}$$

  where ψ is the azimuth angle, φ_0 is the collective pitch, φ_1 and φ_2 are the control parameters, k_β is the pitch-flap coupling, k_ξ is the pitch-lag coupling. Note that the influence of aerodynamic forces on the pitch angle occurs implicitly through the flapping angle and lagging angle.

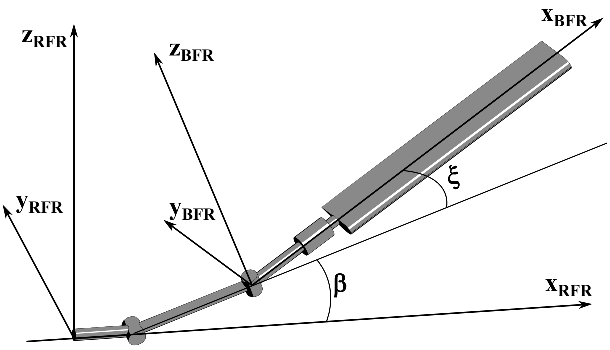

Figure 2. The helicopter frame of reference and the blade frame of reference

The blade movement is considered in the BFR which is defined as follows: the FR origin coincides with the center of LH, the Oz axis is co-directed with the LH axis, the Ox axis is directed along the blade, and the Oy axis complements the FR to the right-hand system (see Fig. 2).

3.3. Governing Equations

Let us denote the current distance from the start of the blade by r and introduce vector $\boldsymbol{g}$ which is the vector of gravity acceleration defined in the BFR. Let us also determine the values of blade mass per unit length as ρ and the aerodynamic force per unit length as $\boldsymbol{q_a}$

$$\rho(r) = \frac{dm(r)}{dr}, \quad \boldsymbol{q}_a(r) = \frac{d\boldsymbol{F}_a(r)}{dr}.$$

Then the equations for finding the angles β, ξ can be written in the form of the following laws of conservation of angular momentum [19].

The equation for flapping hinge is

$$\begin{gathered}\ddot{\beta}\int\limits_0^R ((l_{PH}+r)\cos\xi + l_{LH})^2\rho\, dr = \\ \int\limits_0^R (A_z q_{az} + B_z g_z \rho)\, dr + \int\limits_0^R (C_z\omega^2 + D_z\omega\dot{\xi} + E_z\dot{\beta}\dot{\xi})\rho\, dr.\end{gathered} \tag{3}$$

The equation for lagging hinge is

$$\begin{gathered}\ddot{\xi}\int\limits_0^R (l_{PH}+r)^2\rho\, dr = \\ \int\limits_0^R (A_y q_{ay} + B_y g_y \rho)\, dr + \int\limits_0^R (C_y\omega^2 + D_y\omega\dot{\beta} + E_y\dot{\beta}^2)\rho\, dr.\end{gathered} \tag{4}$$

Here the coefficients $A_z,\ A_y,\ B_z,\ B_y,\ \ldots,\ E_y$ are the nonlinear functions depending on the variables β, ξ.

The terms in the right-hand side of these equations are the moments of forces relative to FH and LH. They can be divided into moments of external and inertial forces. The factors in front of $\ddot{\beta}$ and $\ddot{\xi}$ are the moments of inertia of the considered mass-geometric model of the blade relative to FH and LH

$$J_{FH} = \int_0^R ((l_{PH}+r)\cos\xi + l_{LH})^2\rho\, dr,$$

$$J_{LH} = \int_0^R (l_{PH}+r)^2\rho\, dr.$$

The laws of conservation of angular momentum (3) and (4) can be written in the vector form as

$$\boldsymbol{J}\frac{d\boldsymbol{\omega}_{rel}}{dt} = \boldsymbol{M}_{EXT} + \boldsymbol{M}_I, \tag{5}$$

where $\boldsymbol{J}$ is the tensor of the blade momentum defined as the momentum J_{PH} and J_{LH} referred to PH and LH

$$\boldsymbol{J} = \begin{pmatrix} J_{FH} & 0 \\ 0 & J_{LH} \end{pmatrix}.$$

Here $\boldsymbol{\omega}_{rel} = (\dot{\beta}, \dot{\xi})^{\mathsf{T}}$ is the vector of angular velocities of relative rotation, $\boldsymbol{M}_{EXT} = \left(M_{EXT/FH}, M_{EXT/LH}\right)^{\mathsf{T}}$ is the vector of external forces moments, $\boldsymbol{M}_I = \left(M_{I/FH}, M_{I/LH}\right)^{\mathsf{T}}$ is the vector of inertial forces moments.

The solution of system (5) describes the flapping and lagging motions of the blade assuming that the cyclic pitch and the collective pitch of the rotor are given analytically.

The aerodynamic force vector $\mathbf{F}_a$ is obtained from the solution of RANS equations. Note that it is defined in the absolute HFR and before using in the system of equations (5) it must be projected onto the BFR as

$$\boldsymbol{F}_a^{BFR} = \boldsymbol{A}_{HFR}^{BFR}\boldsymbol{F}_a^{HFR},$$

where $\boldsymbol{A}_{HFR}^{BFR}$ is the transfer matrix.

By solving the system (5), we find the values of the angles and angular velocities β, $\dot{\beta}$, ξ, $\dot{\xi}$ at the next time step, and thereby determine the position of the blade relative to the hinges and the mesh velocity at the next time step.

3.4. Numerical Methods

In general, a system of ordinary differential equations (ODE) can be written in the form

$$\begin{aligned} \ddot{\beta} &= f_\beta(\beta, \dot{\beta}, \xi, \dot{\xi}), \\ \ddot{\xi} &= f_\xi(\beta, \dot{\beta}, \xi, \dot{\xi}). \end{aligned} \tag{6}$$

Let us introduce the new vector $\boldsymbol{Y}$ of unknown components defined as $y_1 = \beta$, $y_2 = \xi$, $y_3 = \dot{\beta} = \dot{y}_1$ and $y_4 = \dot{\xi} = \dot{y}_2$ and denote the right-hand side vector $\boldsymbol{F}$ as

$$\boldsymbol{Y} = \begin{pmatrix} y_1 \\ y_2 \\ y_3 \\ y_4 \end{pmatrix}, \quad \boldsymbol{F} = \begin{pmatrix} F_1 \\ F_2 \\ F_3 \\ F_4 \end{pmatrix} = \begin{pmatrix} y_3 \\ y_4 \\ f_\beta(y_1, y_3, y_2, y_4) \\ f_\xi(y_1, y_3, y_2, y_4) \end{pmatrix}. \tag{7}$$

Then the system (6) can be identically transformed to the first-order autonomous ODE system:

$$\dot{\boldsymbol{Y}} = \boldsymbol{F}(\boldsymbol{Y}). \tag{8}$$

The system (7)–(8) is solved by a multi-step Taylor Series Method. This method is sometimes called the linearized Runge–Kutta method or the Runge–Kutta method with minimal storage [15, 18]. Let $\boldsymbol{Y}^n = \boldsymbol{Y}\left(t^n\right)$, then, according to this method, the unknown vector at the next time step $\boldsymbol{Y}^{n+1} = \boldsymbol{Y}\left(t^n + \Delta t\right)$ is defined as

$$\begin{aligned} &\boldsymbol{Y}^{(0)} = \boldsymbol{Y}^n, \\ &\boldsymbol{Y}^{(k)} = \boldsymbol{Y}^n + \alpha_k \Delta t \boldsymbol{F}(t^n, \boldsymbol{Y}^{(k-1)}), \quad k = 1, \ldots, m, \\ &\boldsymbol{Y}^{n+1} = \boldsymbol{Y}^{(m)}, \end{aligned}$$

where the coefficients α_k are

$$\alpha_k = \frac{1}{m - k + 1}.$$

This multi-step method for a linear autonomous system has the m-th order of accuracy, for a nonlinear system only the second. Note that for small deviation angles β and ξ, the system (7)–(8) can be considered as linear and therefore solved with an order of accuracy equal to the number of integration steps m.

4. Elastic Mesh for Cyclic Pitch Control and Flapping Motions

Previously in [11] we introduced a computational method for simulating the motion and deformation of a body in a fluid or gas dynamic environment, focusing on maintaining the quality of the computational mesh during the body movement. The method is particularly suitable for the problems involving the motions controlled externally and/or by the aerodynamic forces such as the cyclic pitch control and flapping motions of helicopter rotor blades. Due to its ability to handle small displacements and rotations while maintaining mesh quality, it can be effectively applied to simulate the flow around hinged rotors. An articulated blade typically undergoes cyclic pitch, flapping, and lead-lag motions. These movements can be described using the Euler angles and small displacements, which align well with the method assumption of small linear and angular motions.

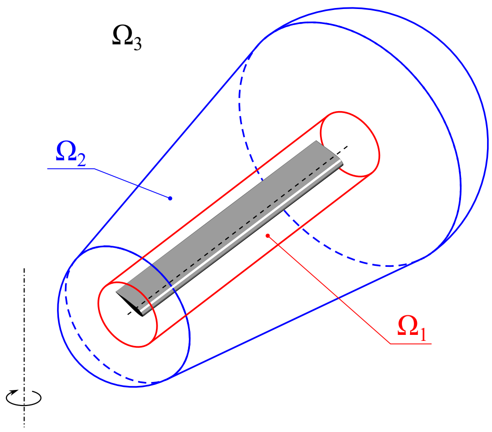

Figure 3. Deformation zones near the rotor blade

Following the method, a computational domain is divided into three subdomains. The first domain Ω_1 contains the rotor blade and its immediate vicinity. The mesh nodes in this region move with the blade, ensuring accurate resolution of the boundary layer and thereby calculation of aerodynamic forces. Domain Ω_3 includes the nodes far from the blade that remain either motionless or rotating with the rotor depending on the chosen FR. Domain Ω_2 is the deformation region where the mesh nodes move to accommodate the blade motion while preserving the mesh topology and quality. The deformation in domain Ω_2 relies on constructing an auxiliary web-structured "strand mesh" which connects the moving and stationary regions via radial strands. An inner surface ($\partial\Omega_1$) is defined around the blade, while the outer surface ($\partial\Omega_2$) is constructed concentrically (see Fig. 3). Elastic radial strands connecting these surfaces allow the mesh to deform smoothly as the blade moves.

The compression-stretching of the auxiliary mesh is controlled by one-dimensional laws acting along each strand and providing smooth changes in the size of mesh cells. Note that this approach requires very little additional computing resources. Moreover, the web structure of strand mesh simplifies the interpolation of flow variables from it to the main unstructured mesh.

The implemented algorithm [11] allows to move nodes in the deformation region according with the blade displacements while maintaining the initial unstructured mesh topology and preventing its tangling. As for the hinged rotor problems, the auxiliary mesh is automatically constructed at the beginning of the computation if the minimum and maximum hinge angles can be defined (see Fig. 4). Then it is used within the whole simulation.

5. Numerical Results

5.1. Pendulum

In the pendulum test, the algorithm implementing the motion of a pendulum under the influence of gravity on a deformable unstructured mesh is verified. In this problem, the combined operation of the implemented rotor blade mechanics and the mesh deformation algorithm are

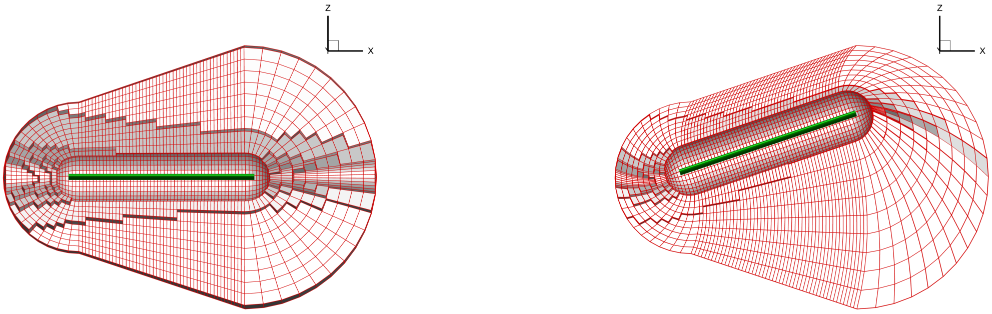

(a) Initial blade strand mesh (b) Deformed blade strand mesh

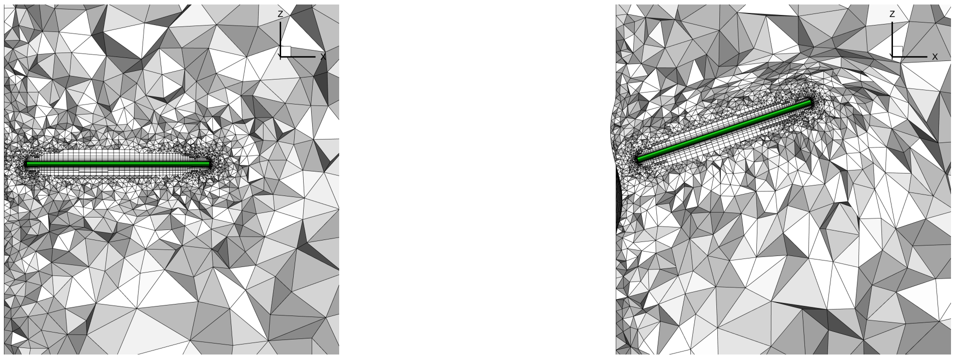

(c) Initial blade computational mesh (d) Deformed blade computational mesh

Figure 4. Strand mesh deformation and corresponding computational mesh deformation

verified without taking into account the impact of aerodynamic forces. The pendulum represents a rigid rod 3 meters long with no hinges. An auxiliary strand mesh is built large enough to cover a region of possible rod deflection of angles up to 20° (see Fig. 5).

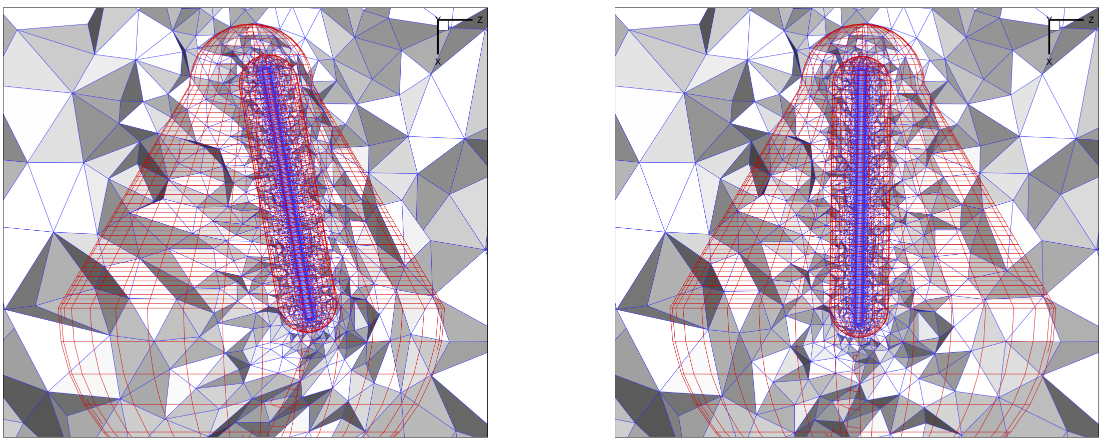

(a) $\beta = \pi/18$ (b) $\beta = 0$

Figure 5. Computational (blue) and strand (red) meshes for pendulum cases

It is assumed that the pendulum is described by set of N different point units with mass m_i located at a distance $r_i,\ i = 1, \ldots,\ N$ from the suspension point. The motion of such pendulum is described by the equation

$$\ddot{\beta} + g\frac{\sum_{i=1}^{N} m_i r_i}{\sum_{i=1}^{N} m_i r_i^2} \sin\beta = 0.$$

If the angle β is assumed small enough and the linearized equation becomes valid, the solution can be given by the formula

$$\beta(t) = \beta(0)\cos\left(\sqrt{g\frac{\sum_{i=1}^{N} m_i r_i}{\sum_{i=1}^{N} m_i r_i^2}}\ t\right).$$

In the first case, the radial velocity $\omega = 0$, the azimuthal blade displacement $\psi = 0$, the zero hinges displacements $l_{VH} = l_{HH} = l_{PH} = 0$, the initial hinges angular velocities $\dot{\beta}(0) = \dot{\xi}(0) = 0$ and the initial pendulum position is set by the deflection angle $\beta(0) = \frac{\pi}{18}$, $\xi(0) = 0$.

The rest case parameters are the following: the mass distribution: $dm_i\left(\frac{r_i}{R}\right) = \begin{bmatrix} 0.25 & 1 \\ 1\ \text{kg} & 1\ \text{kg} \end{bmatrix}$, the pendulum length $R = 3$ m, the gravity acceleration $\boldsymbol{g} = (9.8, 0, 0)$ m/s^2.

For the given parameters, the solution for a small flapping angle is:

$$\beta(t) = \frac{\pi}{18}\cos\left(\sqrt{\frac{9.8 \cdot 5}{17}}\ t\right). \tag{9}$$

Figure 6 shows a comparison of the numerical solution with the analytical one (9) for the linearized equation. It can be seen that the solutions coincide in amplitude, but there is a little phase discrepancy between the numerical solution and the exact solution of linear equation. The magnitude of this error decreases with decreasing the initial angle of deflection, otherwise, with the diminishing influence of nonlinearity.

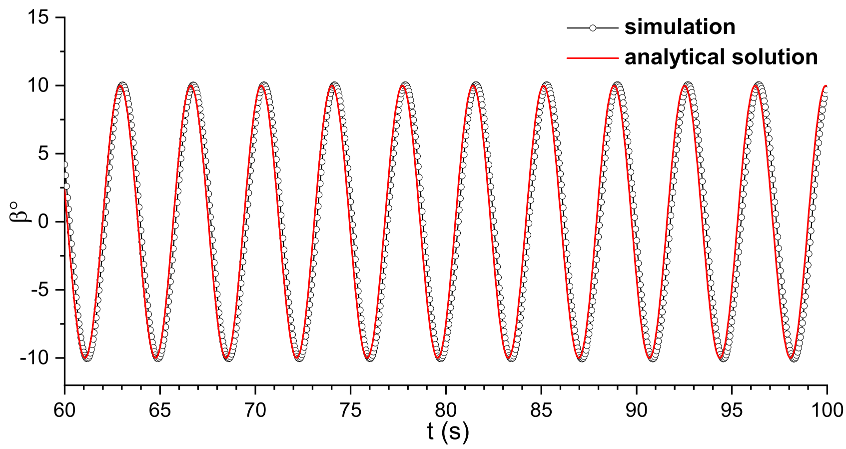

Figure 6. Evolution of deflection angle for pendulum

5.2. Rod Rotation Cases

In the following two cases, the algorithm implementing the motion of a rotating rigid body under the influence of inertial forces on a deformable unstructured mesh is verified. The configuration setup is the following: the radial velocity $\omega = 1$ rad/s, the azimuthal blade displacement $\psi = 0$, the hinges displacements $l_{HH} = 10$ m, $l_{VH} = l_{PH} = 0$, the hinges angular velocities: $\beta(0) = 0.02\pi$, $\dot{\beta}(0) = 0.01\pi$ rad/s, $\xi(0) = \dot{\xi}(0) = 0$ and no gravity acceleration $\boldsymbol{g} = (0, 0, 0)$. The blade length is 3 m and the mass distribution of single point unit is $dm_i\left(\frac{r_i}{R}\right) = \begin{bmatrix} 0.5 \\ 2\ \text{kg} \end{bmatrix}$.

Analytically, for small angles, the motion in terms of the evolution of the angle β under the action of centrifugal forces due to the rotation is described by the equation:

$$\ddot{\beta} + (1+\epsilon)\,\omega_e^2\beta = 0,$$

where $\epsilon = 1 + S_{HH} \cdot l_{HH}/J_{HH}$, $S_{HH} = \sum dm_i(l_{VH} + (l_{PH} + r_i)\cos\xi)$ is the center of mass of the rod along the Oy_{BCS} axis, and $J_{HH} = \sum dm_i(l_{VH} + (l_{PH} + r_i)\cos\xi)^2$ is the moment of inertia of the rod relative to the Oy_{BCS} axis. This linear equation has the following solution:

$$\beta\,(t) = \beta_0 \cos\left(\omega_e t\sqrt{1+\epsilon}\right) + \frac{\dot{\beta}_0}{\omega_e\sqrt{1+\epsilon}} \sin\left(\omega_e t\sqrt{1+\epsilon}\right)$$

or, for the given configuration:

$$\beta\,(t) = 0.02\pi \cos\left(t\sqrt{3}\right) + \frac{0.01\pi}{\sqrt{3}} \sin(t\sqrt{3}).$$

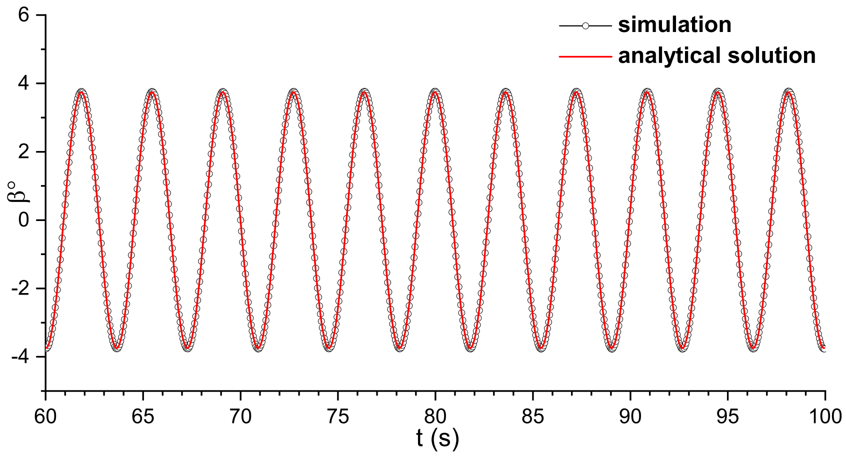

Figure 7. Evolution of rotating rod flapping angle

Figure 7 demonstrates a comparison of the numerical solution with the analytical one of the linear equation. It can be seen that the numerical solution practically coincides with the exact solution.

Now let us consider the test on the motion of the rod in terms of the angle ξ determining its lead-lag movement. The test configuration is similar to the previous one except the hinges angular velocities given as $\beta\,(0) = \dot{\beta}\,(0) = 0$, $\xi\,(0) = 0.02\pi$, $\dot{\xi}\,(0) = 0.01\pi$ rad/s.

For small angles, the lead-lag motion is analytically described by the following equation:

$$\ddot{\xi} + \nu^2\omega_e^2\xi = 0,$$

where $\nu^2 = S_{VH}(l_{HH} + l_{VH})/J_{VH}$, $S_{VH} = \sum dm_i\,(l_{PH} + r_i)$ is the center of mass of the rod along the Oz_{BCS} axis, and $J_{VH} = \sum dm_i\,(l_{PH} + r_i)^2$ is the moment of inertia of the rod relative to the Oz_{BCS} axis. This linear equation has the following solution:

$$\xi\,(t) = \xi(0)\cos\left(\nu\omega_e t\right) + \frac{\dot{\xi}(0)}{\nu\omega_e} \sin\left(\nu\omega_e t\right)$$

or, for the given configuration:

$$\xi\,(t) = 0.02\pi \cos\left(t\sqrt{1.6}\right) + \frac{0.01\pi}{\sqrt{1.6}} \sin\left(t\sqrt{1.6}\right).$$

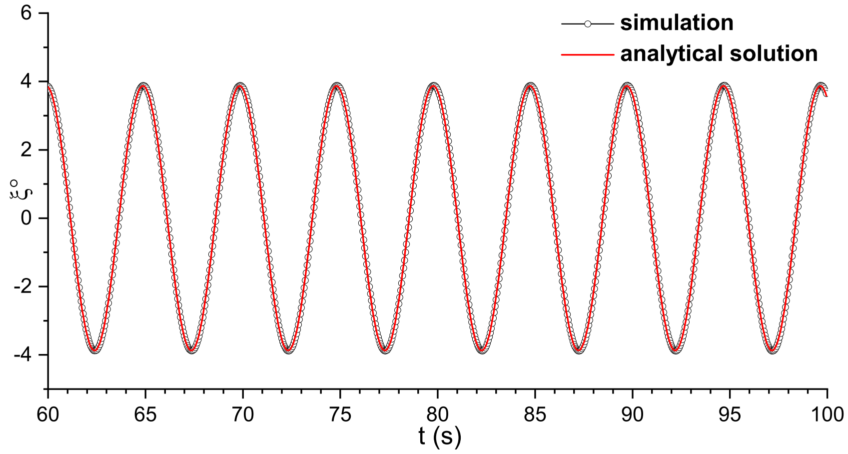

Figure 8. Evolution of rotating rod lead-lag angle

In Fig. 8, a comparison between the numerical solution and the analytical one of the linear equation is shown. As in case of the flapping angle, the numerical and exact solutions are practically indistinguishable.

5.3. Model Hinged Rotor in Hover

In this case, the algorithm implementing the flapping motion of an articulated blade and the work of flap hinge under the influence of aerodynamic forces on a deformable unstructured mesh is verified. During the rotation of the hinged rotor, the FH allows the blades to freely perform flapping motions. Over time, the flapping angle, the same for all the blades, should stabilize, forming a taper of the rotor.

In the test case under consideration, the flow around a hinged rotor with two hinged blades, rectangular in plan and made on the basis of NACA0012 airfoil without twist, is simulated. The rotor radius is 1.142 meters, and the blade chord is 0.1903 meters with the aspect ratio equal to 6. The pitch angle is fixed at 8°. The horizontal hinges are located at a distance of 0.05 meters from the rotor axis, which allows the blades to perform flapping movements. Each blade has mass of 1 kg, the center of mass is located in the middle of the blade mid-span. The rotational speed is 650 RPM, corresponding to the tip speed of 77.7 m/s and the tip Mach number of 0.23. The environmental parameters are chosen to ensure a Reynolds number of 10^4, reducing the requirements for boundary layer cell height to satisfy the condition $y^+ < 1$. The Reynolds number is determined using a viscosity coefficient of 0.0413 Pa·s. The flow simulation is based on solving the RANS equations with the SA turbulence model.

At the pre-processing stage, the deformation zone covered with the strand mesh is automatically built for each blade (see Fig. 9, left). The inner cylindrical part contains the blade surface with the surrounding boundary layer elements (hexahedrons and triangular prisms).

The computational domain represents a cylindrical region with the diameter and height of 60 meters and the axis coinciding with the rotor axis. An unstructured mesh is constructed on the blade surface, and the prismatic boundary layer consisting of hexahedrons and triangular prisms is then built starting from the surface, transitioning isotropically to tetrahedrons with increasing the distance from the surface. The near wall cell size is chosen to ensure the condition $y^+ < 1$. The computational mesh in whole contains 2.8×10^5 nodes and 8.6×10^5 volume elements (see Fig. 9, center, right).

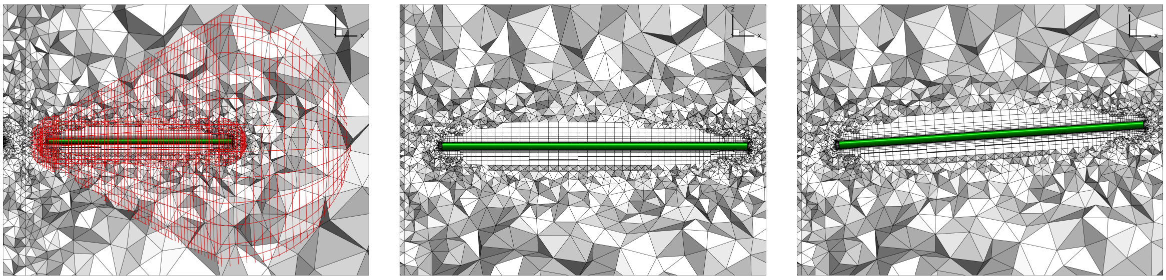

(a) Initial computational and strand meshes

(b) Computational mesh, flapping angle 0

(c) Computational mesh, flapping angle 3.7°

Figure 9. The mesh pattern near the blade: the strand mesh and the unstructured computational mesh deformations

During the computation, at each time step, the aerodynamic forces acting on the blade are calculated based on the pressure distribution on the blade surface. These forces are fed to the input of the algorithm of the hinged rotor mechanics. The angular velocities of the blade motion are determined basing on the current force distribution along the blade span with considering the presence of hinges. Then, on the base of the location on the current time step and the angular velocities, the new position of the blade is calculated.

Within the computation after 20 revolutions, the thrust, torque, and coning angle of the rotor stabilize and reach the steady-state values (see Fig. 10, where vertical lines indicate the beginning of each rotor revolution).

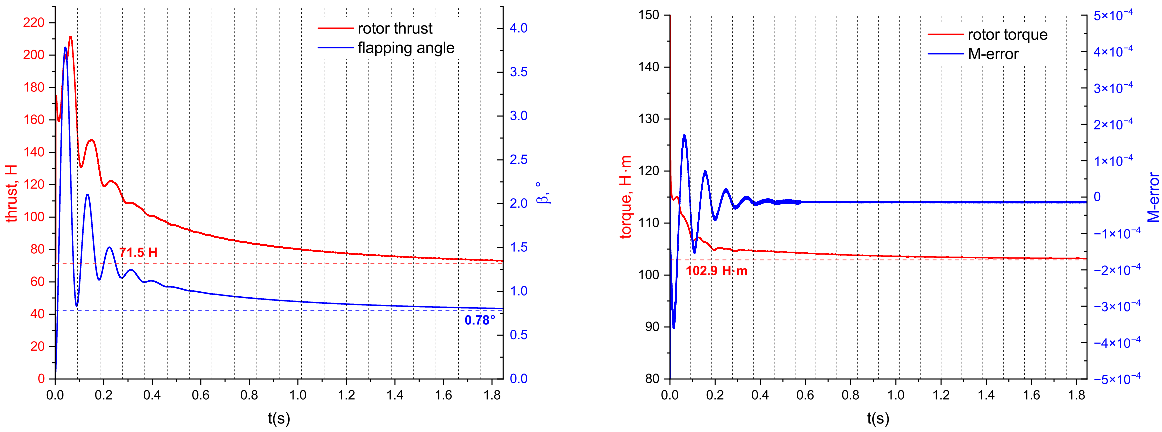

(a) Thrust and flapping angle

(b) Moment and relative error

Figure 10. Two-bladed rotor characteristics evolution

To assess the reliability of the numerical result, one can check the fulfillment of the equilibrium condition at specific moments in time from the perspective of d'Alembert's principle. In the considered problem formulation, from the standpoint of this principle, the following forces act on the blade: the gravitational force, the aerodynamic force, and the inertial force, which consists of the terms arising from the rotation with the speed ω and the acceleration $\ddot{\beta}$. The equilibrium condition in the hinge is written as:

$$-M_\omega - M_g + M_{AD} - M_{\ddot{\beta}} = 0,$$

where $M_{\ddot{\beta}} = J \cdot \ddot{\beta}$ and J is the moment of inertia of the blade relative to the hinge.

The values of the moments of inertial forces and gravitational force M_ω, M_g and $M_{\ddot{\beta}}$ can be determined from the blade configuration and the data on its spatial position. To determine the moment of aerodynamic forces relative to the hinge, it is necessary to evaluate it in the BFR and integrate it with respect to the corresponding level arm length (for details see [19]).

These equilibrium equations are checked for each simulation time step. The measure of the discrepancy is estimated as

$$M_{err} = \frac{M_{AD} - M_\omega - M_g - M_{\ddot{\beta}}}{|M_{AD}|}.$$

The result is presented in Fig. 10b. The maximum relative error M_{err} in the equilibrium equation is less than 4×10^{-4}. This error corresponds to a change in the blade mass in the current configuration of approximately 0.1%, from which it can be concluded that the equilibrium is maintained and the algorithm is implemented correctly.

5.4. Model Hinged Rotor in Forward Flight

In this test case, the computation exploits the whole computational method including the mesh deformation algorithm, and the algorithms implemented the hinged rotor blade mechanics and turbulent flow simulation. The case represents the simulation of the flow around a model hinged rotor in forward flight. In such flight regime, the cyclic collective pitch control intended to reduce the aerodynamic force and moment oscillations is required. Thus, the test problem is considered in a setup with the cyclic pitch control and free flapping motions of the blades in the horizontal hinge.

Let us consider the model hinged rotor of four articulated blades. Each blade is based on NACA23012 airfoil with linear twist. The rotor radius is 2.442 meters, and the blade chord is 0.16 meters. The horizontal hinges are located on the rotor axis and allow the blades to perform flapping motions. The distribution of elementary masses along the blade span is given in Tab. 1.

Table 1. Four-bladed rotor mass distribution

r/R	0.0335	0.0570	0.0887	0.1673	0.2137	0.2636	0.3219	0.3721
m, kg	0.9111	0.8146	0.2585	0.1831	0.1345	0.1427	0.1333	0.1311
r/R	0.4291	0.5431	0.6572	0.7712	0.8292	0.8683	0.9116	0.9541
m, kg	0.2507	0.3066	0.2866	0.1937	0.1050	0.0876	0.0890	0.1392

The rotational speed of 840 RPM is constant with the tip velocity of 215 m/s corresponding to the tip Mach number of 0.63. The environmental parameters are as follows: the air density is 1.2051 kg/m^3, the pressure is 101325 Pa. The Reynolds number calculated based on the blade chord and the tip speed is 2.7×10^6. The flow simulation is carried out by numerically solving the RANS equations with the closing SA turbulence model.

The simulation of turbulent flow around the helicopter rotor in forward flight takes into account the complex curvilinear motion of the articulated blades. In this setup, the rotor angle of attack is zero, the upstream flow velocity is 60 m/s, and the blade pitch angle at the section $r/R = 0.7$ is $\varphi_0 = 12.6°$ (or 11.1° with the pitch-flap coupling, see the details below). The cyclic pitch control is governed by the following law for the blade azimuthal position ψ:

$$\varphi(\psi) = \varphi_0 + a_1 \sin\psi + b_1 \cos\psi + k\beta, \tag{10}$$

where the coefficients have the following values: $\varphi_0 = 12.6°$, $a_1 = -4.5°$, $b_1 = 1°$, $k = -0.5$.

The computational mesh is constructed in such a way that the initial blade pitch angle corresponds to the law (10) at the initial time moment with the flapping angle $\beta = 5°$. Thus, the initial blade pitch angle in the mesh is set to $\varphi(\psi = 0, \beta = 5°) = 11.1°$. Note that this step is not mandatory as the blade is positioned correctly through the mesh deformation at the initial stage of the computation; however, such mesh prescription improves the robustness and expands the limitations of the mesh deformation algorithm.

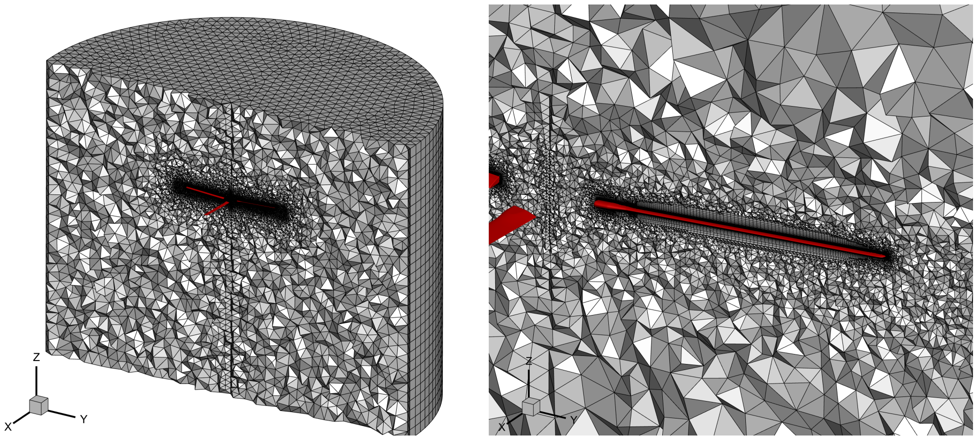

Figure 11. Computational mesh for the model four-bladed hinged rotor

As in the previous case, the unstructured mesh is constructed on the blade surface, and a prismatic boundary layer consisting of hexahedrons and triangular prisms is built starting from the surface and transitioning isotropically to tetrahedrons with increasing the distance from the surface (see Fig. 11). The nearwall cell size is chosen to ensure the condition $y^+ < 1$. The constructed computational mesh contains 4.8×10^6 nodes and 9×10^6 volume elements.

To reach a quasi-steady state, eight full rotor revolutions are needed. As practice shows, in the presence of an upstream flow (under the oblique flow conditions), it is enough to reach a periodicity of the aerodynamic characteristics. The evolution of thrust and torque confirms this (see Fig. 12).

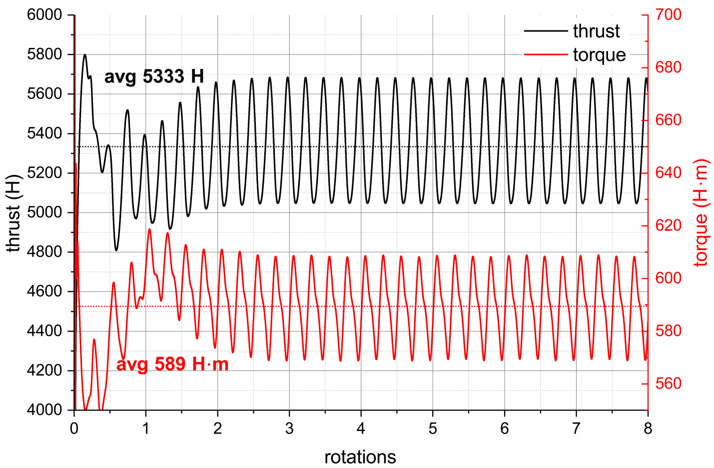

Figure 12. Evolution of four-bladed rotor thrust and torque

The overall flow pattern obtained by the simulation meets the expectations: the turbulent wake and tip vortices are carried downstream; the largest regions of negative gauge pressure are observed on the surface of the advancing blade while the smallest ones are on the blade moving downstream (Fig. 13).

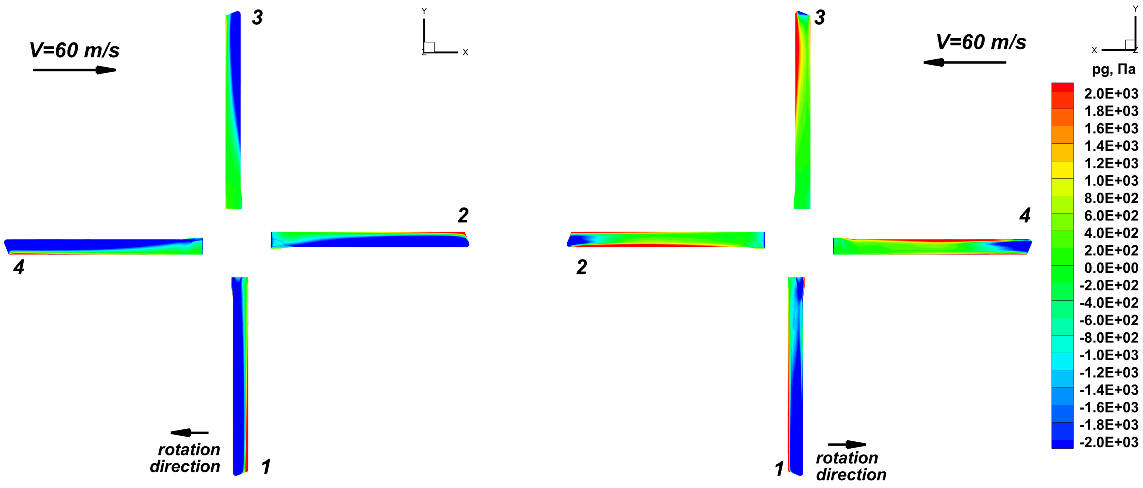

(a) Rotor upper surface

(b) Rotor lower surface

Figure 13. Gauge pressure distribution

Figure 13 shows the distribution of gauge pressure on the upper and lower surfaces of the rotor. As expected, the region of low pressure is the largest on the surface of the advancing blade (1) making the greatest contribution to rotor thrust at this azimuth. The last is well seen in the blade and rotor thrust charts (Fig. 14). The thrust maxima correspond to the azimuth of 82° and the multiples of them in 90° increment. Similarly, the thrust minima occur at the azimuth of 34° and the multiples thereof with a step of 90°.

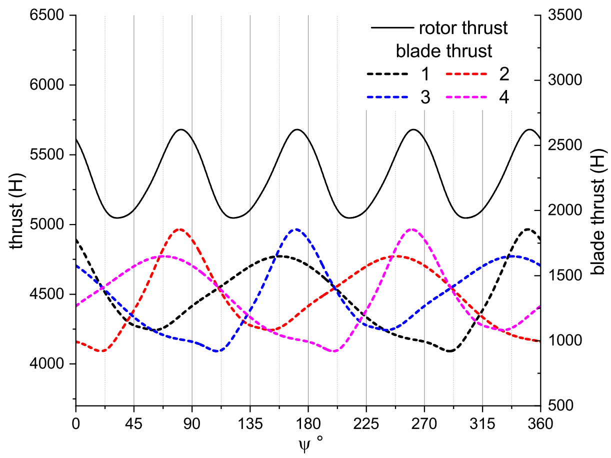

Figure 14. Distribution of rotor and blades thrust over one rotor revolution

Note that the deviation from the average thrust and torque values (and, consequently, their coefficients, see Fig. 15a) does not exceed 4.2% and 2.1%, respectively. Additionally, the influence of cyclic control leads to a significant reduction of the amplitude of fluctuations in the transverse and lateral forces, as expected (see Fig. 15b, where c_T is the thrust force coefficient, c_H is the horizontal force coefficient and c_S is the side force coefficient).

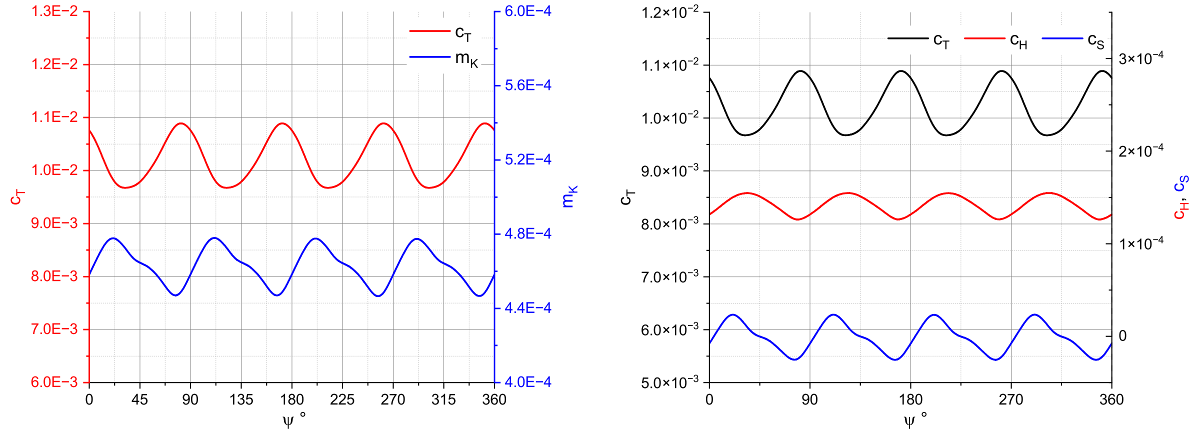

(a) The thrust and torque coefficients

(b) The coefficients of aerodynamic forces

Figure 15. Distribution of rotor aerodynamic and force coefficients over one rotor revolution

Conclusion

This paper presents a way of numerically simulating the turbulent flow near a helicopter hinged rotor, i.e., the rotor consisting of articulated rigid blades. As practice shows, accounting for hinged-blade motions within its rotation is extremely needed for designing new helicopters since it may strongly contribute to their aerodynamic and acoustic properties. At the same time, from a computational point of view, taking these movements into account significantly complicates the numerical simulation. The latter is built basing on an efficient coupling of high-fidelity computational gas dynamics and mechanics of hinged blades, and requires special computational techniques to implement it. In particular, robust economic solutions are needed to provide the proper mobility of a hinge blade under the action of inertial forces, gravity and external cyclic control. The resulting complete computational algorithm is one way or another highly resource-intensive, so the use of high-performance supercomputers is in great demand for solving such problems.

In the future, the authors intend to develop this method, to continue its verification and validation, and to extend it to the case of interacting helicopter rotors both for co-axial and spaced apart formulations.

Acknowledgements

The research is carried out using the equipment of the shared research facilities of HPC computing resources at Lomonosov Moscow State University [22], and Shared Resource Center of KIAM RAS `http://ckp.kiam.ru`.

References

1. MBDyn - Multi-Body Dynamics. `https://www.mbdyn.org`

2. Abalakin, I., Bakhvalov, P., Kozubskaya, T.: Edge-based reconstruction schemes for unstructured tetrahedral meshes. International Journal for Numerical Methods in Fluids 81(6), 331–356 (2016). https://doi.org/10.1002/fld.4187

3. Abalakin, I.A., Bobkov, V.G., Kozubskaya, T.K.: Numerical study of fuselage impact on acoustic characteristics of a helicopter rotor. Supercomputing Frontiers and Innovations 9(4), 100–113 (Dec 2022). https://doi.org/10.14529/jsfi220409

4. Abalakin, I.V., Bobkov, V.G., Kozubskaya, T.K., *et al.*: Numerical simulation of flow around rigid rotor in forward flight. Fluid Dynamics 55(4), 534–544 (Jul 2020). https://doi.org/10.1134/S0015462820040011

5. Abalakin, I.V., Bakhvalov, P.A., Bobkov, V.G., *et al.*: Noisette CFD&CAA supercomputer code for research and applications. Supercomputing Frontiers and Innovations 11(2), 78–101 (aug 2024). https://doi.org/10.14529/jsfi240206

6. Altmikus, A.R.M., Wagner, S., Beaumier, P., Servera, G.: A comparison: Weak versus strong modular coupling for trimmed aeroelastic rotor simulations. In: AHS International, 58th Annual Forum Proceedings. vol. 1, pp. 697–710 (2002), https://api.semanticscholar.org/CorpusID:125998085

7. Bakhvalov, P.A., Kozubskaya, T.K.: EBR-WENO scheme for solving gas dynamics problems with discontinuities on unstructured meshes. Computers and Fluids 157, 312–324 (2017). https://doi.org/10.1016/j.compfluid.2017.09.004

8. Bakhvalov, P.A., Kozubskaya, T.K., Rodionov, P.V.: EBR schemes with curvilinear reconstructions for hybrid meshes. Computers and Fluids 239(105352) (2022). https://doi.org/10.1016/j.compfluid.2022.105352

9. Bakhvalov, P.A., Surnachev, M.D.: Method of averaged element splittings for diffusion terms discretization in vertex-centered framework. Journal of Computational Physics 450(110819), 110819 (2022). https://doi.org/10.1016/j.jcp.2021.110819

10. Bakhvalov, P.A., Vershkov, V.A.: Edge-based schemes on moving hybrid meshes in the NOISEtte code. Keldysh Inst. Appl. Math. Preprint 127 (2018). https://doi.org/10.20948/prepr-2018-127

11. Bobkov, V.G., Vershkov, V.A., Kozubskaya, T.K., Tsvetkova, V.O.: Deformation technique of unstructured mesh deformation to find the aerodynamic characteristics of bodies at small displacements. Mathematical Models and Computer Simulations 13(6), 986–1001 (Nov 2021). https://doi.org/10.1134/s2070048221060028

12. Gorobets, A., Bakhvalov, P.: Heterogeneous CPU+GPU parallelization for high-accuracy scale-resolving simulations of compressible turbulent flows on hybrid supercomputers. Computer Physics Communications 271, 108231 (Dec 2022). https://doi.org/10.1016/j.cpc.2021.108231

13. Gorobets, A.V., Duben, A.P.: Technology for supercomputer simulation of turbulent flows in the good new days of exascale computing. Supercomputing Frontiers and Innovations 8(4), 4–10 (Dec 2021). https://doi.org/10.14529/jsfi210401

14. Ilkko, J., Hoffren, J., Siikonen, T.: Simulation of a helicopter rotor flow. Journal of Structural Mechanics 43(3), 186–205 (2011). https://doi.org/10.1016/j.jcp.2021.110819

15. Jameson, A.: Numerical solution of the Euler equations for compressible inviscid fluids. In: Angard, F., *et al.* (eds.) Numerical methods for the Euler equations of Fluid Dynamics, pp. 199–245. SIAM (1985)

16. Johnson, W.: Rotorcraft aerodynamics models for a comprehensive analysis. In: Proceedings of the 54th Annual Forum of the American Helicopter Society. vol. 2, pp. 1184–1206. Curran Associates, American Helicopter Society International, Washington, D.C. (May 1998)

17. Kopiev, V.F., Zaytsev, M.Yu., Vorontsov, V.I., *et al.*: Helicopter noise in hover: Computational modelling and experimental validation. Acoustical Physics 63(6), 686–698 (Nov 2017). https://doi.org/10.1134/s1063771017060070

18. Lallemand, M.H.: Dissipative properties of Runge-Kutta schemes with upwind spatial approximation for the Euler equations, Research Report RR-1173, INRIA (1990), https://inria.hal.science/inria-00075385

19. Lipatov, A.V., Abalakin, I.V.: The hinged rotor mechanics. Keldysh Institute Preprints (8), 1–24 (2025), https://library.keldysh.ru/preprint.asp?id=2025-8

20. Steijl, R., Barakos, G., Badcock, K.: A framework for CFD analysis of helicopter rotors in hover and forward flight. International Journal for Numerical Methods in Fluids 51(8), 819–847 (Jan 2006). https://doi.org/10.1002/fld.1086

21. van der Ven, H., Boelens, O.J.: A framework for aeroealistic simulations of trimmed rotor systems in forward fight. In: European Rotorcraft Forum, Marseille, September 1416 (2004)

22. Voevodin, Vl., Antonov, A., Nikitenko, D., *et al.*: Supercomputer Lomonosov-2: Large scale, deep monitoring and fine analytics for the user community. Supercomput. Front. Innov. 6(2), 4–11 (2019). https://doi.org/10.14529/jsfi190201

23. Vorontsov, V.I., Faranosov, G.A., Karabasov, S.A., Zaitsev, M.Yu.: Comparison of the noise directivity pattern of the main rotor of a helicopter for flight and hover modes. Acoustical Physics 66(3), 303–312 (may 2020). https://doi.org/10.1134/s1063771020030082

24. Xu, L., Weng, Pf.: Rotor wake capture improvement based on high-order spatially accurate schemes and chimera grids. Applied Mathematics and Mechanics 32(12), 1565–1576 (Dec 2011). https://doi.org/10.1007/s10483-011-1523-6

25. Zhang, Z., Qian, Y.: Unsteady RANS/DES analysis of flow around helicopter rotor blades at forword flight conditions. Modern Physics Letters B 32(12n13), 1840015 (2018). https://doi.org/10.1142/S0217984918400158